








Cite this: *Nanoscale*, 2024, **16**, 614

Direct synthesis of CsPbX₃ perovskite nanocrystal assemblies†

Chujie Wang,^a Sri K. Matta,^{b,c} Chun Kiu Ng,^{b,c} ^a Chang Cao,^a Manoj Sharma, ^{*a}
 Anthony S. R. Chesman, ^d Salvy P. Russo ^b and Jacek J. Jasieniak ^{*a}

Inorganic CsPbX₃ (X = Cl, Br, I) perovskite nanocrystals (NCs) possess many advantageous optoelectronic properties, making them an attractive candidate for light emitting diodes, lasers, or photodetector applications. Such perovskite NCs can form extended assemblies that further modify their bandgap and emission wavelength. In this article, a facile direct synthesis of CsPbX₃ NC assemblies that are 1 μm in size and are composed of 10 nm-sized NC building blocks is reported. The direct synthesis of these assemblies with a conventional hot-injection method of the NCs is achieved through the judicious selection of the solvent, ligands, and reaction stoichiometry. Only under selective reaction conditions where the surface ligand environment is tuned to enhance the hydrophobic interactions between ligand chains of neighbouring NCs is self-assembly achieved. These assemblies possess narrow and red-shifted photoluminescence compared to their isolated NC counterparts, which further expands the colour gamut that can be rendered from inorganic perovskites. This is demonstrated through simple down-converting light emitters.

Received 26th August 2023,
 Accepted 17th November 2023

DOI: 10.1039/d3nr04285e

rsc.li/nanoscale

Introduction

Inorganic CsPbX₃ (X = Cl, Br, I) perovskite nanocrystals (PNCs) have attracted great research interest because of their high photoluminescence quantum yield (PLQY),¹ narrow photoluminescence (PL) emission full-width half-maximum (FWHM),² defect-tolerant band structure,³ and readily tunable emission wavelength across the visible spectrum.⁴ PNCs are typically synthesized by a colloidal method, stabilized with long-chain hydrocarbon ligands, and possess good solution processability.⁵ With all these advantageous properties, PNCs have demonstrated promise in applications such as light-emitting diodes (LED),⁶ lasers,⁷ photodetectors,⁸ and solar cells.⁹ To support these applications, ongoing research into PNCs is needed around structurally controlled nanoparticles and their assemblies, both in solution and in suitable host matrices.

While the study of direct PNC synthesis is prominent,¹⁰ the formation of NC assemblies requires more attention.

NCs assembled into ordered structures are known as supercrystals (SCs). Such assemblies can modify their optoelectronic properties,¹¹ inducing narrower emission linewidths, coherent superfluorescence, and increased stimulated emission.^{12–15} To date, the main approaches for assembling NCs into such assemblies include: (1) direct synthesis through ultrasonication and elevated precursor concentration;¹² (2) slowly evaporating the solvent of previously synthesized and monodisperse PNC dispersions;¹³ (3) introducing polar anti-solvents or complexing agents into a PNC dispersion to drive assembly;^{16,17} and (4) post-synthesis ligand exchange.¹⁸ The assembly of perovskites is not limited to cube shaped NCs, with reports extending the assembly of perovskites to other morphologies, such as nanoplatelets (NPLs),¹⁹ nanorods,²⁰ and nanosheets.²¹ However, with the exception of ultrasonication,¹² SC assembly methods have been limited largely to two-step processes, requiring initial hot-injection synthesis of PNC dispersions and a separate, subsequent, assembly method.

The synthesis of PNC assemblies has been largely reliant on inter-molecular forces, namely hydrogen bonding, dipole-dipole interactions (*i.e.* van der Waals forces, VdW),²² or electrostatic attractions.²³ In contrast, the role of hydrophobic interactions, which are an inherent feature of alkyl ligand-stabilized NC systems, have not been well understood in the direct synthesis of PNC-SCs.²⁴ For gold nanoparticles, the

^aARC Centre of Excellence in Exciton Science, Department of Materials Science and Engineering, Monash University, Clayton, Victoria 3800, Australia.

E-mail: manoj.sharma@monash.edu, jacek.jasieniak@monash.edu

^bARC Centre of Excellence in Exciton Science, School of Science, RMIT University, Melbourne 3000, Australia

^cCenter for Computational Sciences, University of Tsukuba, Japan

^dCSIRO Manufacturing, Ian Wark Laboratories, Research Way, Clayton, VIC 3168, Australia

† Electronic supplementary information (ESI) available: Details of computational methods, supporting figures of DLS, TEM, XRD, SADP, UV-vis absorption, NMR, etc. See DOI: <https://doi.org/10.1039/d3nr04285e>

hydrophobic interaction between the long chain hydrocarbon capping ligands on the nanoparticle surface has been reported to effectively modulate their assembly.²⁵ The hydrophobic interaction originates from the tendency of two hydrophobes (*e.g.* hydrocarbon ligands) to mutually attract, resulting in the rearrangement of nearby solvent molecules, and hence increasing the system's overall entropy. The strength of the hydrophobic interaction can be an order of magnitude larger than the van der Waals force, and is dependent on two primary factors: (1) the length and shape of the hydrophobes, with long and straight hydrocarbon chains ensuring greater hydrophobicity and less steric hindrance, giving rise to stronger hydrophobic interaction; and (2) the polarity of the solvent, with more polar solvents decreasing the solubility of the hydrophobes, leading to increased hydrophobic interaction.²⁶ Although PNCs are typically capped with long-chain hydrocarbon ligands (*e.g.* oleic acid, OLA, and oleylamine, OLA), their assembly into SCs by intrinsic hydrophobic interactions has not yet been reported.

Herein, a facile direct synthetic method for perovskite SCs of CsPbCl₃, CsPbBr₃, and CsPbI₃ is reported. The SCs are up to 1 μm in size and are assembled from 10 nm-sized NC building blocks during the hot-injection synthesis. The synthesis of the SCs follows the conventional hot-injection method of the PNCs, with slight modifications to the solvent, ligands, and stoichiometry employed in the reaction. It is found that these tailored reaction conditions enhance the effective hydrophobic interactions between the PNCs to drive their assembly into SCs. The degree of this hydrophobic interaction is manipulated by modifying the ligand hydrocarbon chain structure and length, which eventually influences the SC's formation. Optical characterization of these SCs show greatly red-shifted PL emission and narrowed PL FWHM. Such CsPbX₃ PNC-SCs are further shown to be readily introduced into hybrid polymer-SC matrices that can be used within colour-tunable down-converting light-emitting devices.

Methods

Materials

Cesium carbonate (Cs₂CO₃, 99.995% trace metal basis), lead(II) chloride (PbCl₂, 99.999% trace metals basis), lead(II) bromide (PbBr₂, 99.999% trace metals basis), lead(II) iodide (PbI₂, 99.999% trace metal basis), dodecane (anhydrous, ≥99%), 1-octadecene (ODE, 90%, technical grade), oleylamine (OLA, 70%, technical grade), octylamine (99%), hexadecylamine (HDA, 98%), octadecylamine (97%), hydrochloric acid (ACS reagent, 37 wt% in H₂O), hydroiodic acid (57 wt% in H₂O, distilled, stabilized, 99.95%), polymethyl methacrylate (PMMA, MW~350 000), and toluene (99.5%, analytical reagent), were purchased from Sigma-Aldrich. Isopropanol (IPA, 99.5%, analytical reagent), hexane (99.5% analytical reagent), and hydrobromic acid (48 wt% in H₂O, ≥99.99%) were purchased from Merck. Dodecylamine (98%) was purchased from Alfa Aesar. Bis(2,4,4-trimethylpentyl) phosphinic acid (TMPPA,

85%) was purchased from Cytec. All reagents were used without further purification.

Synthesis

Synthesis of Cs precursor solution. The reaction was carried out using a standard Schlenk line. Cs₂CO₃ (0.1 g, 307 μmol) was suspended in a solution of dodecane (5 ml) and TMPPA (0.5 ml) in a 50 mL three-neck flask, and placed under high vacuum (1 mbar) with stirring for 1 h to remove residual moisture. The suspension was then heated to 140 °C under N₂, with the temperature being maintained until all the Cs₂CO₃ had fully dissolved. The solution remained homogeneous when cooled to room temperature (RT), and was stored under N₂. The temperature of the solution was raised to 120 °C before use.

Synthesis of CsPbX₃ nanocrystals (NCs). The reaction was carried out using a standard Schlenk line. PbX₂ (188 μmol, 52 mg PbCl₂, 69 mg PbBr₂, 87 mg PbI₂) was suspended in a solution of ODE (5 mL), TMPPA (0.5 mL), and OLA (0.5 mL) in a 50 mL three-neck flask (for PbCl₂, both TMPPA and OLA volumes are increased to 1 mL), and heated to 120 °C under vacuum (1 mbar) with stirring, with the temperature maintained for 1 h. After dissolution of the PbX₂, the temperature of the reaction solution was increased to 140 °C under N₂. Then, 0.4 mL of the preheated Cs precursor solution was injected into the reaction solution, and after 5 s the flask was submerged in a water bath to quench the reaction. The crude CsPbX₃ NC solution in ODE was mixed with anti-solvent IPA in a 1 : 3 (v/v) ODE : IPA ratio. The mixture was then centrifuged for 5 min at 10 000 rpm in a Beckman Coulter AllegraTM X-22R Centrifuge. The supernatant was discarded, and the CsPbX₃ NC precipitate was redispersed in hexane.

Synthesis of CsPbX₃ supercrystals (SCs). The reaction was carried out using a standard Schlenk line. PbX₂ (188 μmol, 52 mg PbCl₂, 69 mg PbBr₂, 87 mg PbI₂) was suspended in a solution of dodecane (5 mL), TMPPA (1 mL), HDA (760 mg) and HX (366 μmol, 28 μL HCl, 34 μL HBr, 40 μL HI) in a 50 mL three-neck flask, and placed under high vacuum (1 mbar) with stirring for 1 h. Then, the temperature was raised to 140 °C under N₂. After all the PbX₂ were dissolved, 1.6 mL of the preheated Cs precursor solution was injected into the reaction solution, and after 5s the flask was submerged in a water bath to quench the reaction. The crude CsPbX₃ SC solution in dodecane was then centrifuged for 5 min at 10 000 rpm. The clear supernatant was discarded, and the CsPbX₃ SC precipitate was redispersed in hexane.

Preparation of SC-PMMA composite. PMMA beads were mixed in toluene at a concentration of 200 mg mL⁻¹ and stirred overnight for full dissolution. 100 μL of the SC solution (concentration ~4.8 × 10⁻⁶ M) was then mixed with 2 mL of the PMMA solution, and then transferred to a circular Teflon mould with a 1.5 cm radius. The Teflon mould was then placed in a desiccator with a low vacuum applied to remove the solvent over 12 h. The SC-PMMA composites were then removed from the mould and stored in ambient condition.

Characterizations

UV-Vis spectroscopy. UV-Vis absorbance spectra were collected using a PerkinElmer Lambda 950 UV-Vis-NIR spectrometer. For solutions, 10 μl of either the NC (concentration $\sim 1.2 \times 10^{-6}$ M) or SC (concentration $\sim 4.8 \times 10^{-6}$ M) solution was diluted in 3 ml of hexane inside a 1 cm pathlength glass cuvette. For films, NC or SC solutions were drop cast on thin glass slides and the solvent was evaporated under ambient conditions.

Optical characterizations. Photoluminescence spectra were collected using a Horiba Fluoromax-4 spectrofluorometer. The excitation wavelength was 360, 440, 520 nm for the CsPbCl_3 , CsPbBr_3 , and CsPbI_3 samples, respectively. The solution concentration or film preparation was the same as the absorption measurement. Time-resolved photoluminescence (TRPL) and photoluminescence quantum yields (PL QYs) were measured by a FluoTime 300 time-correlated single photon counting (TCSPC) system (Pico Quant Co., Ltd, Berlin, Germany).

X-ray diffraction (XRD). Samples were prepared for XRD measurements by drop casting solutions of NC or SC in hexane on a glass substrate. XRD patterns were acquired on a Bruker D8 Advance diffractometer using a Cu source ($K\alpha = 1.54 \text{ \AA}$) at 40 kV, 40 mA, and a LynxEye detector.

Transmission electron microscopy (TEM). TEM and high-resolution transmission electron microscopy (HRTEM) images, High-angle annular dark-field imaging (HAADF), selected area diffraction patterns (SADP), and STEM-Energy Dispersive X-ray (EDX) mapping were obtained on a FEI Tecnai G2 F20 S-Twin transmission electron microscope equipped with a field emission gun electron source operated at 200 kV. Images were acquired by either an Orius SCD200D wide-angle CCD camera or a Gatan Ultrascan 1000 high-resolution CCD camera. EDX was obtained by a Bruker X-Flash X-ray detector with an energy resolution of 123 eV.

For TEM sample preparation, 10 μl of either the NC or SC solutions were diluted in 1 ml of hexane, and the TEM sample grid (Ted Pella inc. ultrathin carbon film) was immersed into the mixture and the solvent was then evaporated.

Nuclear magnetic resonance spectroscopy (NMR). ^{31}P NMR measurements were performed on a Bruker Bio Spin Av400H with a 9.4 T magnet and a 5 mm inverse 1H-X BBI autotuning broadband probe at a 1H frequency of 400.13 MHz. All samples were measured in d_8 -toluene.

Computational methods

Periodic Density Functional Theory (DFT) calculations were performed using the Vienna *Ab initio* simulation package (VASP) software platform.^{27,28} For all calculations (geometry optimizations and single point energy) the Perdew–Burke–Ernzerhof (GGA-PBE) exchange–correlation functional with the associated Projector-Augmented-Wave (PAW) pseudopotentials were used.^{29,30} The planewave cut-off was 400 eV or 550 eV in different models of the study but maintained the consistency of the cut-off within the same system analysis. As the supercell sizes used in this study were large (more than 400 atoms),

Gamma point sampling was used to sample the Brillouin Zone (BZ). The convergence criteria for electronic convergence and ionic relaxation loop convergence was 10^{-5} eV and 10^{-4} eV, respectively. In the aperiodic (surface) direction a minimum vacuum space of 20 \AA was used to minimize interactions with periodic images of the supercell in that direction. Grimme's scheme was also used to incorporate van der Waals's interactions.^{30,31} The 3D model visualisation is done using VESTA software.³²

Results and discussion

Synthesis of CsPbX_3 supercrystals

As shown in Fig. 1a, our synthesis of CsPbX_3 generally follows a modified hot-injection method developed by Kovalenko *et al.*,¹ in which Cs_2CO_3 and PbX_2 precursors are dissolved separately in solutions containing ligands, with the Cs-precursor subsequently being injected into the PbX_2 mixture at 140 $^\circ\text{C}$ to yield the nanocrystalline products. These products are isolated *via* centrifugation with the addition of a polar anti-solvent and then redispersed in hexane. As per our previous report, bis-(2,2,4-trimethylpentyl) phosphinic acid (TMPPA, chemical formula in Fig. S1†) has been used as the acidic ligand to produce stable cubic-phase CsPbI_3 .³³ Herein, the CsPbI_3 system was also used as an example to demonstrate the synthesis of normal NCs and self-assembled SCs. When the conventional unsaturated solvent (octadecene, ODE) and amine ligand (OLA) are used with the TMPPA, monodisperse cubic-phased CsPbI_3 NCs are synthesised (Fig. 1b–d). However, upon modifying the reaction stoichiometry of the Cs, Pb and I precursors, utilising saturated (aliphatic) solvent (dodecane) and an amine ligand (hexadecylamine, HDA), direct synthesis of CsPbI_3 SCs could be achieved (Fig. 1e–g). The effects of these two modifications will be discussed shortly.

As seen from transmission electron microscopy (TEM) images (Fig. 1g), the assemblies of CsPbI_3 within the SCs are on the 0.1–1 μm scale, which is comparable to the reported CsPbBr_3 SCs.^{12,17} Such a larger size of the CsPbI_3 SCs is further confirmed through dynamic light scattering (DLS) measurements, which show significantly larger mean sizes ($\sim 1 \mu\text{m}$, Fig. S2†) for the SCs, compared with the typical 10–100 nm for normal NC dispersions. Additional TEM and HAADF images at different magnifications are provided in Fig. S3 and S4.† At low magnification (Fig. S3a†), isolated NCs can still be observed in the sample, however, the SCs comprise the majority of the product. When inspected at a higher magnification (Fig. S3c†), a periodic inter-connected morphology comprising of the ~ 10 nm sized NC building blocks can be clearly identified. This alignment of the NC building blocks suggests that assembly occurs due to a ligand-directed process.¹³ SADP of these SCs proves that the individual NCs are cubic-phased, while also providing evidence of preferential orientations within the assemblies (Fig. 1f inset). Notably, when changing the halide component from iodide to bromide and chloride, the respective CsPbBr_3 and CsPbCl_3 SCs can also



Fig. 1 (a) Schematic illustration of CsPbX₃ NC and SC syntheses. Structure illustration, low and high magnification TEM images for (b)–(d) CsPbI₃ NCs and (e)–(g) SCs. Insets of (c) and (f) are indexed SADP of NCs and SCs.

be achieved. Energy Dispersive X-ray (EDX) elemental mapping and X-ray Diffraction (XRD) patterns are included in the SI for the Cl, Br, and I SC analogues. As shown by EDX mapping, the Cs, Pb, and X elements are evenly distributed throughout the SCs (Fig. S5†). The corresponding XRD patterns have been further indexed to their perovskite phases (Fig. S6†).

A distinct feature of directly synthesised SCs is that they can be purified from the crude reaction solution *via* centrifugation without any anti-solvent. As a result of their size, when redispersed in hexane and stored, the SCs spontaneously precipitate, leaving a colourless supernatant. Such a stronger sedimentation effect of the SCs is in stark contrast with the OLA-capped NCs, which form stable dispersions in hexane. Considering the similar chain length and a functional binding group of HDA and OLA, we believe the SC formation to arise from the different steric and/or hydrophobic interactions provided by these ligands (*vide infra*). Notably, it has been previously shown that NCs capped with lecithin ligands enable concentrated dispersions without precipitation or formation of SCs.⁴⁵ Lecithin ligands provide multi-dentate surface coordination and strong steric hindrance to enable these dispersion properties. Therefore, to overcome these strong repulsive steric interactions, the potential role of strong hydrophobic interactions observed for the saturated straight-chained HDA (or its ammonium salt) used in this work needs to be understood.

A critical parameter affecting the formation of SCs is reactant stoichiometry. Experiments were conducted in which the concentration of the Cs and I ratios were increased relative to a fixed amount of Pb precursor through the addition of Cs precursor or hydroiodic acid as an iodine source. TEMs presented in Fig. 2 illustrate the effect of tuning the reactant stoichiometry. In a conventional hot injection synthesis of NCs, a Cs:Pb:I molar ratio of 1:4:8 yields monodisperse cube-shaped NCs (Fig. 2a).¹ When the Cs content is doubled, the

majority of the NCs retain the same morphology; however, a small portion of hexagonal-shaped particles also form (Fig. 2b). Meanwhile, a four-fold increase in Cs content yields only hexagonal shape particles (Fig. 2c), which are ascribed to the Cs₄PbI₆ phase according to the indexing of the SADP (Fig. S7†). This phase has been reported to form at high Cs:Pb ratios.³⁴ Doubling the iodide content of the original reaction stoichiometry did not change the morphology of the product (Fig. 2d). However, at this elevated iodide ratio and progressively higher Cs content, >100 nm ordered nanocrystalline assemblies formed (Fig. 2e and f).

To further explain the effect of stoichiometry on SC formation, the reaction yield of the synthesis was determined. For this, the concentration of CsPbI₃ NCs was first calculated using the UV-vis absorption spectra of the samples shown in Fig. 2d–f (Fig. S8†) and our previously reported extinction coefficient of CsPbI₃ NCs,³⁵ with the reaction yield being subsequently determined by considering Cs as the limiting reagent (see ESI†). The NC reaction yields across these samples were all around 70–85% (Table S1†). Moreover, the CsPbI₃ concentration increased almost four-fold (1.1×10^{-6} M to 4.8×10^{-6} M) for the 1:1:4 sample as compared to the conventional 1:4:8 stoichiometry. Such a high CsPbI₃ concentration is in accordance with a previous report that a high NC concentration is essential for SC formation.¹²

Another critical factor determining direct SC formation is that the solvent and ligand systems used must be saturated hydrocarbons. Firstly, replacing the saturated solvent dodecane with the conventional unsaturated solvent ODE under otherwise identical reaction conditions for CsPbI₃ SCs synthesis results in no SCs forming (Fig. S9†). This observation is consistent with the additional iodide content provided by the hydroiodic acid being consumed through an additional reaction with the double bond of the ODE, which is in great

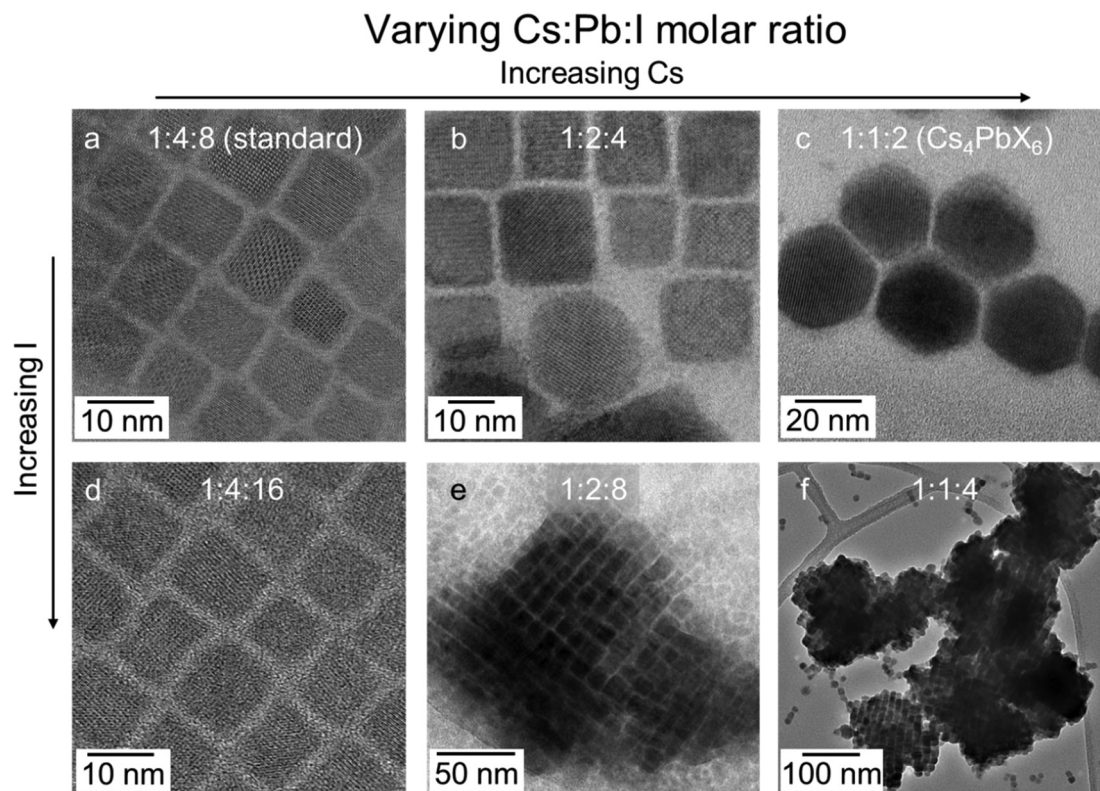


Fig. 2 TEM images of CsPbI₃ NCs synthesised using HDA-HI at different Cs:Pb:I molar ratios: (a) 1:4:8, (b) 1:2:4, (c) 1:1:2, (d) 1:4:16, (e) 1:2:8, and (f) 1:1:4. All images were taken immediately after synthesis.

excess.³⁶ Secondly, to differentiate between the use of saturated and unsaturated solvent and ligand systems, syntheses were carried out using various ligand combinations. As a starting point, a comparison of both the conventional OLA and the straight chained HDA ligands was made. The OLA produced well-dispersed nanocubes without any evidence of SC formation (Fig. S10†). Similarly, if the TMPPA in the SC reactions is replaced by the conventionally-used OLA, SCs also do not form (Fig. S11†). Instead, polydisperse nanocube structures are observed, which can be attributed to the fact that OLA is binding to the NCs' surface.³⁷

The use of TMPPA in an otherwise conventional synthesis of NCs results in surface chemistry that is dominated by alkyl amine/ammonium salts.³³ ³¹P NMR spectroscopy indicates that this holds true for SCs formed within a saturated dodecane solvent and HDA ligand system, for which the presence of phosphorous-containing species in purified solutions of CsPbCl₃, CsPbBr₃ and CsPbI₃ SCs cannot be detected (Fig. S12†). Therefore, it can be concluded that a surface chemistry composed of straight-chained HDA and/or its ammonium derivative are an essential aspect to the formation of the SCs.

To probe this further, TEM was used to measure the inter-NC distance of NCs synthesized using HDA and OLA ligands. Again, because the TMPPA is not present at the surface, the amine and/or its ammonium species should be the dominating surface ligand contributor. As seen in Fig. 3(a and b) the

inter-NC distance for the HDA sample, either in the NC or the SC form, is determined to be around 2 nm. This is consistent with the fully extended chain length of HDA (2.18 nm),³⁸ indicating that the HDA ligands likely interdigitate between adjacent NC surfaces. Such a configuration would ensure close contact of the hydrocarbon chains of HDA, thus favouring stronger hydrophobic interactions,²⁴ which can further support the assembly of NCs into SCs. In comparison, the distance between the OLA-capped NCs is ~2.5 nm (Fig. 3c), which is much larger than the extended chain length of an OLA molecule (2.0 nm). This is consistent with the bent OLA possessing a higher degree of rotational freedom, which reduces the extent that it can interdigitate.³⁹ As a result, decreased hydrophobic interactions would be expected for OLA ligand passivation. While it has been shown that OLA surface chemistry supports SC formation, it requires ultra-high NC concentrations or narrow NC size distributions to enhance their for their formation.^{12,13}

DFT modelling

To further support the hypothesis of ligand-interdigitation-induced SC formation, Density Functional Theory (DFT) calculations of a CsPbI₃ perovskite surface with a PbI₂ terminated (001) surface interacting with OLA-X and HDA-X surface ligands were performed (Fig. 4a–c). Previous studies on gold nanoparticle assemblies have indicated that the attachment

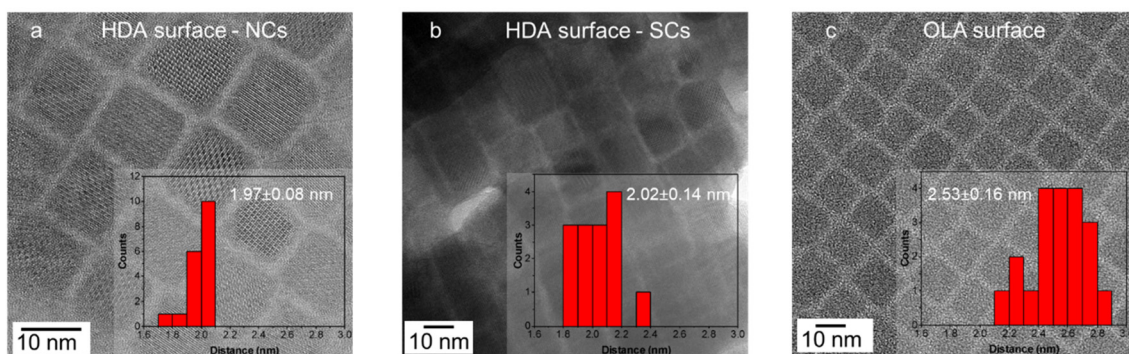


Fig. 3 TEM images and histograms for the measurement of the inter-NC surface distance for (a) HDA-Br capped NCs, (b) HDA-Br capped SCs, (c) OLA-Br capped NCs.

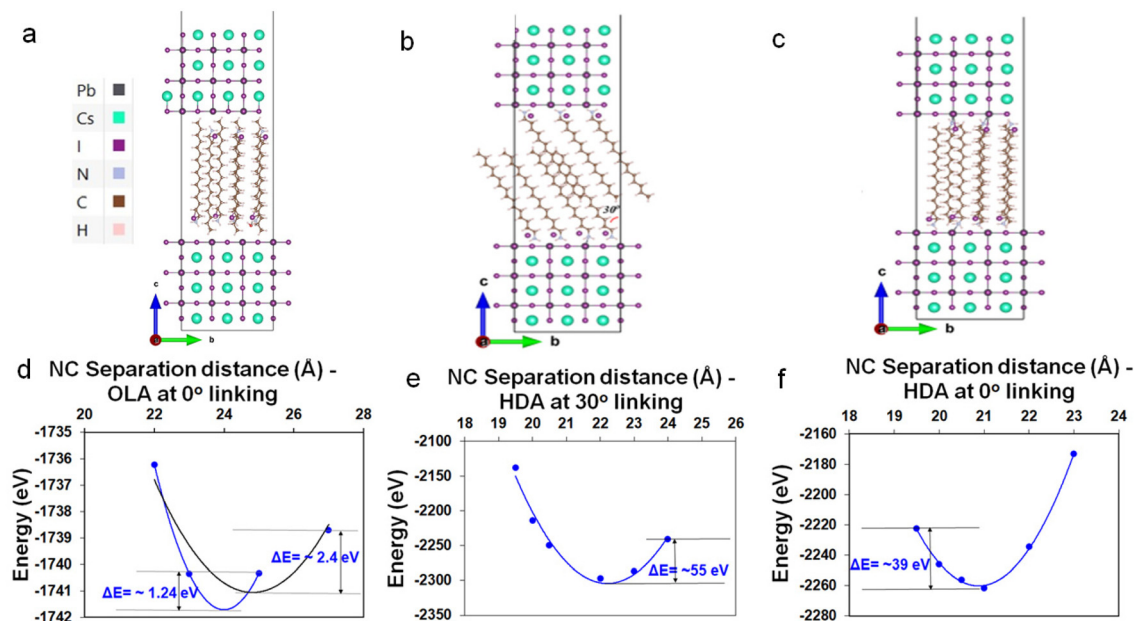


Fig. 4 (a) 2×1 supercell of six-layered CsPbI_3 NCs facing each other with OLA linked on PbI_2 terminated (001) surfaces on both NCs at 0° angle with c -lattice direction. Similarly, (b and c) a 3×1 supercell with I linked at 30° and 0° with respect to c -lattice direction. The colour code for the atoms in models are: Cs (cyan), I (purple), Pb (black), N (light blue), C (brown), and H (pale purple). In the orientation given, the Pb atoms are partially obscured by the I atoms. Calculation of DFT energy (in eV) for (d) OLA and, (e and f) HDA ligands linked to nanoparticles as a function of NC separation distance (in Angstrom) at 30° and 0° with respect to c -lattice direction. The dashed lines are quadratic polynomial fits to the data as a visual guide.

angle between alkylamine ligands and the vertical c -axis of the nanoparticle is between 0° and 30° ,⁴⁰ whereas for the HDA ligand this angle has been experimentally and computationally determined to be 30° .⁴¹ While this provides a gauge into the bonding nature typical of such native ligands, the partial quaternization of the amine to form the ammonium salt within the synthesis of perovskites necessitates an understanding of the alkyl ammonium bromide salts.

Our DFT calculations indicate that OLA-X has the lowest energy configuration with an attachment angle of 0° , while for the HDA-X ligand angle configurations of both 0° and 30° present the lowest energy configurations (Fig. S13†). Under

these bonding conditions, the average ligand density is calculated to be 3.15 and 2.94 ligands per nm^2 for the OLA-X and HDA-X ligands, respectively, which is a similar ligand density to that obtained experimentally of ~ 3 ligands per nm^2 .³⁵

We further explore the total energy dependence on the distance (d), between two such passivated perovskite surfaces (see Fig. 4d–f as a guide). For OLA-X, the ligands have a 0° link, which made it very difficult to obtain converged DFT energies at various separation distances. Therefore, we were only able to obtain converged results for 4 distance values; 2.2, 2.3, 2.5, and 2.7 nm (Fig. 4d). Meanwhile, for the two HDA-X ligand configurations (30° and $\sim 0^\circ$), we were able to obtain converged

DFT energies for 6 distance values, ranging between 1.95–2.4 nm (Fig. 4e and f). We would expect the potential energy surfaces in these systems to have a complex multidimensional structure with hills, valleys, and saddle points. However, if we assume that the reaction path coordinate corresponding to the vertical separation distance between the NPs is one that would be associated with large energy variations in the ground electronic state, then the surface energy may look approximately parabolic about the atomic equilibrium positions of this coordinate. Assuming this to be the case, then under the harmonic approximation the separation distance corresponding to the local potential minima (*i.e.* the equilibrium separation distance) could be approximated as a distance associated with the well minimum. Therefore, in Fig. 4d–f, we have fitted the potential energy profile to a quadratic polynomial fit to approximate the equilibrium NP separation distance. This distance would be the most probable distance of separation between any two NCs in the system at ground-state if the assumptions stated above hold.

For OLA-X (Fig. 4d) we fitted the data to a parabolic fit using the first 3 data points (blue line) and all 4 data points (black line). The calculated values of the equilibrium separation distance for these fits were 2.4 (blue) and 2.48 (black). Therefore, we believe the true value lies within this range. For the HDA-X coated NCs, the local minimum in the potential energy surface is approximately 2.09 nm for the 0° attached ligand (Fig. 4f) and slightly larger at 2.22 nm for the 30° attached ligand (Fig. 4e). Both of these results are in very good agreement with the experimental results. Notably, the deeper potential energy well for the 30° attachment model *versus* the 0° attachment suggests that the preferred ligand bonding angle is different for HDA-X compared to the OLA-X ligands.

Effect of hydrophobic interactions

When NCs prepared using the 1 : 4 : 8 Cs : Pb : I stoichiometry with HDA surface ligands were stored under ambient conditions, they exhibited a gradual self-assembly into SCs over time. As shown in Fig. 5a and b, immediately after synthesis and purification, the sample contained well dispersed NCs, whereas after 10 days of storage at ambient condition, the UV-

vis absorption spectrum (Fig. 5c) of this sample showed an increase in scattering over time, indicating the formation of SCs. Also, the PL peak of this sample red-shifted during this time, accompanied by a decrease in low wavelength emission. This is consistent with the progressive enhancement of particle electronic coupling and cascading energy transfer in the evolving SCs.³ These results suggest that the hydrophobic interaction is universal for all the NCs with the same HDA ligand environment, and it is sufficiently strong to drive SC formation even at low NC concentrations in hexane.

Phenomenologically, when NCs come into contact due to Brownian motion, ligand chains can intertwine, inducing attractive hydrophobic interactions through dispersive forces.^{42,43} These attractive interactions can be considered through the simplified version of Salem's equation:⁴²

$$E = \frac{A3\pi L}{8\lambda^2 d^5} \quad (1)$$

where E is the attractive dispersive interaction energy between ligand chains, A is the Hamaker constant (0.5×10^{-19} J),⁴⁴ L is length of molecular overlap, λ is length of the basic unit (methylene unit, 0.127 nm) and d is the close-packing distance.

According to Salem's Equation, the similarity of the packing densities for both OLA and HDA in our system, indicates that the molecular overlap length is the primary factor that dictates the major differences in the attractive interactions between our NCs. From the TEM results and the accompanying DFT, nearly full intercalation for HDA-capped NCs and partial intercalation for OLA-capped NCs are observed. Based on the overlap regions, approximated as 2.03 nm (16 methylene groups) and 1.14 nm (9 methylene groups), respectively, we determine the attractive interaction of the HDA-passivated NCs to be ~ 1.8 times larger than those featuring OLA. The enhanced hydrophobic interaction of the HDA-passivated NCs is evidently large enough to overcome the repulsive colloidal interactions existing at room temperature within the hexane solvent. In contrast, the bent hydrocarbon tail of the unsaturated OLA ligands weakens the chain-to-chain interaction to induce dominant inter-particle steric interactions, which

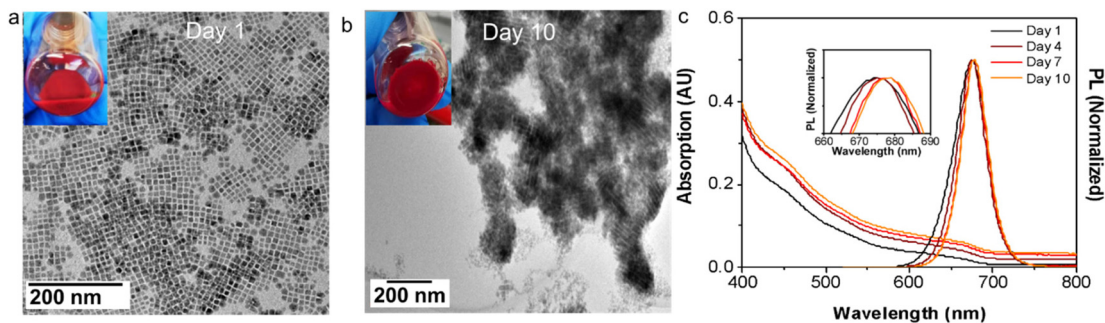


Fig. 5 TEM images and photos for the CsPbI₃ crude solution synthesised with Cs : Pb : I = 1 : 4 : 8 stoichiometry that is (a) as-synthesised, (b) stored for 10 days, and (c) evolution of corresponding UV-vis absorption and PL spectra with time (inset: zoom-in PL spectra showing the redshift of the PL peaks).

result in stable colloidal dispersions. Notably, the attractive interactions for OLA-passivated NCs can be enhanced through increased concentrations and/or the addition of polar solvents, to selectively drive aggregation or self-assembly.^{15,16,26,45}

Optical properties

Having examined the SC formation, the optical properties of the SCs are now considered. When SCs are formed, the electronic wavefunctions of the constituent NCs can overlap with each other for sufficiently small inter-particle distances, leading to enhanced electronic coupling.⁴⁶ Meanwhile, the dense NC packing in SCs also leads to an increased local dielectric constant, which strengthens the screening of the coulombic interactions. These effects can reduce the exciton binding energy, slow PL recombination and induce PL red-shifting.^{46–48}

The UV-vis absorption and PL spectra of drop-cast CsPbCl₃, CsPbBr₃ and CsPbI₃ SC films are compared with the corresponding NC films in Fig. 6a–c. All the SC samples demonstrate a greater degree of scattering in their absorption spectra, a red shifted PL, and a narrower PL FWHM. Specifically, compared with their NC analogues, a PL red shift of 36 meV, 41 meV, and 59 meV, and a reduced PL FWHM of 12 meV, 13 meV, and 21 meV are observed for the Cl, Br and I SCs, respectively. To further probe these samples, PL, PLQY and TRPL measurements are conducted on the CsPbBr₃ NCs and SCs dispersed in solution and as drop cast films (Fig. S14 and S15[†]). The PL spectra of the SCs in solution and film form show a redshift

compared to the NC analogues, with the redshift being smaller in solution (~24 meV) as compared to films (~51 meV). Meanwhile, the PLQYs for the samples in solution (film) were respectively determined to be 83% (35%) and 51% (32%) (Fig. S14[†]). Finally, TRPL measurements show that the average photoluminescence lifetime for the SCs (~3.5 ns) remains similar compared to the NCs (~3.9 ns) when measured in solution, while increasing in film form from 7.4 ns to 12.8 ns, respectively, due to an enhancement in the long lifetime component (Fig. S15 and Tables S2–S3[†]). While these collective results suggest that strong electronic coupling within the samples is unlikely (significant lifetime reductions expected), without further lower temperature and power-dependent measurements, it is not possible to distinguish between dielectric effects, photon propagation effects (self-absorption) and/or surface impurities.^{12,46,48,49}

A comparison of the emission wavelengths of the NCs and SCs on the colour gamut spectrum shows the red-shifted PL of the SCs slightly extends the range of emission colour beyond what can be rendered from conventional inorganic PNCs (Fig. 6d). For that reason, they are potential candidates for light emitting components and LEDs. As a preliminary proof of concept, SC-PMMA composite films were fabricated as per previous reports,¹ and used as down-converters for commercially available UV LED torches (Fig. 6e). The peak PL wavelength for these SC-composite LEDs is at 414 nm, 522 nm and 700 nm for the Cl, Br and I PNC samples, respectively. While detailed studies are needed to fully quantify and understand



Fig. 6 UV-vis absorption and PL spectra for NC and SC films of (a) CsPbCl₃, (b) CsPbBr₃ and (c) CsPbI₃. (d) The emission of the NCs and SCs plotted on the colour gamut spectrum (CIE 1976); the PL is transformed into the UV through the chromaticity application in Origin software. (e) The PL spectra of the down-conversion LED devices fabricated from the SC-PMMA composites (left) and photos of the LEDs (right).

the origins of the red shifted PL of the SCs as compared to NCs and control the assembly of SCs in solution and film forms, these results do showcase the facile nature of such SC materials as filters for achieving wide colour-gamut tunable LED emission profiles.

Conclusions

In conclusion, we have reported the facile direct synthesis of CsPbX₃ perovskite supercrystals of around 1 μm in size that consist of 10 nm NC building blocks. The synthesis follows the well developed hot injection method, albeit with the conventional unsaturated solvent and ligands replaced with saturated analogues, and the stoichiometry of the precursors tuned to increase the concentration of the NCs. It is experimentally shown and verified through Density Functional Theory that smaller inter-particle distances are observed between NCs containing saturated vs. unsaturated alkyl amine ligands of similar chain length, with only the former yielding SC formation. These factors suggest that enhanced hydrophobic interactions within the saturated ligand system arising from greater interchain overlap provides the dominant driving force for NC assembly. The SCs demonstrate red-shifted absorption and PL, as well as narrowed PL linewidth compared to the discrete NC analogues. These were conducive to achieving expanded colour-gamut down-conversion prototype light-emitting devices. Overall, the facile synthesis of SCs presented here opens a new strategy to manipulate the assembly of PNCs into ordered structures through engineering of the reaction conditions and resulting surface chemistry.

Conflicts of interest

There are no conflicts to declare.

Acknowledgements

This work was funded by the Australian Research Council funded Center of Excellence in Exciton Science (CE170100026). We thank the staff in Monash Center for Electron Microscopy, Monash X-ray platform, and CSIRO NMR facility for their support. This work was also supported by computational resources provided by the Australian Government through the National Computational Infrastructure National Facility and the Pawsey Supercomputer Centre. S. K. M. acknowledges the computing system resources' support from the University of Tsukuba, Japan through the International Postdoctoral Fellowship of Japan Society for the Promotion of Science (JSPS)'s KAKENHI (Grant No. JP22F32733), during part of the computational work and finalization of this study. S. K. M. also acknowledges the FUJITSU Supercomputer PRIMEHPC FX1000 and FUJITSU Server PRIMERGY GX2570 (Wisteria/BDEC-01) facilities at the Information Technology

Center, The University of Tokyo. We acknowledge Elliott Ayers for help during the editing stages of the manuscripts.

References

- 1 L. Protesescu, S. Yakunin, M. I. Bodnarchuk, F. Krieg, R. Caputo, C. H. Hendon, R. X. Yang, A. Walsh and M. V. Kovalenko, *Nano Lett.*, 2015, **15**, 3692–3696.
- 2 A. Swarnkar, R. Chulliyil, V. K. Ravi, M. Irfanullah, A. Chowdhury and A. Nag, *Angew. Chem.*, 2015, **127**, 15644–15648.
- 3 J. Kang and L. W. Wang, *J. Phys. Chem. Lett.*, 2017, **8**, 489–493.
- 4 G. Nedelcu, L. Protesescu, S. Yakunin, M. I. Bodnarchuk, M. J. Grotevent and M. V. Kovalenko, *Nano Lett.*, 2015, **15**, 5635–5640.
- 5 Q. A. Akkerman, M. Gandini, F. Di Stasio, P. Rastogi, F. Palazon, G. Bertoni, J. M. Ball, M. Prato, A. Petrozza and L. Manna, *Nat. Energy*, 2017, **2**, 16194.
- 6 J. Song, J. Li, X. Li, L. Xu, Y. Dong and H. Zeng, *Adv. Mater.*, 2015, **27**, 7162–7167.
- 7 Y. Wang, X. Li, J. Song, L. Xiao, H. Zeng and H. Sun, *Adv. Mater.*, 2015, **27**, 7101–7108.
- 8 Z. Dai, Q. Ou, C. Wang, G. Si, B. Shabbir, C. Zheng, Z. Wang, Y. Zhang, Y. Huang, Y. Dong, J. J. Jasieniak, B. Su and Q. Bao, *J. Mater. Chem. C*, 2019, **7**, 5954–5961.
- 9 A. Swarnkar, A. R. Marshall, E. M. Sanehira, B. D. Chernomordik, D. T. Moore, J. A. Christians, T. Chakrabarti and J. M. Luther, *Science*, 2016, **354**, 92–95.
- 10 C. K. Ng, C. Wang and J. J. Jasieniak, *Langmuir*, 2019, **35**, 11609–11628.
- 11 Z. Nie, A. Petukhova and E. Kumacheva, *Nat. Nanotechnol.*, 2010, **5**, 15–25.
- 12 Y. Tong, E. P. Yao, A. Manzi, E. Bladt, K. Wang, M. Döblinger, S. Bals, P. Müller-Buschbaum, A. S. Urban, L. Polavarapu and J. Feldmann, *Adv. Mater.*, 2018, **30**, 1801117.
- 13 G. Rainò, M. A. Becker, M. I. Bodnarchuk, R. F. Mahrt, M. V. Kovalenko and T. Stöferle, *Nature*, 2018, **563**, 671–675.
- 14 D. Lapkin, C. Kirsch, J. Hiller, D. Andrienko, D. Assalauova, K. Braun, J. Carnis, Y. Y. Kim, M. Mandal, A. Maier, A. J. Meixner, N. Mukharamova, M. Scheele, F. Schreiber, M. Sprung, J. Wahl, S. Westendorf, I. A. Zaluzhnyy and I. A. Vartanyants, *Nat. Commun.*, 2022, **13**, 1–10.
- 15 Z. Liu, X. Qin, Q. Chen, T. Jiang, Q. Chen and X. Liu, *Adv. Mater.*, 2023, **35**, 2209279.
- 16 J. S. Van Der Burgt, J. J. Geuchies, B. Van Der Meer, H. Vanrompay, D. Zanaga, Y. Zhang, W. Albrecht, A. V. Petukhov, L. Fillion, S. Bals, I. Swart and D. Vanmaekelbergh, *J. Phys. Chem. C*, 2018, **122**, 15706–15712.
- 17 K. H. Wang, J. N. Yang, Q. K. Ni, H. B. Yao and S. H. Yu, *Langmuir*, 2018, **34**, 595–602.
- 18 Y. Nagaoka, K. Hills-Kimball, R. Tan, R. Li, Z. Wang and O. Chen, *Adv. Mater.*, 2017, **29**, 1606666.

- 19 S. K. Mehetor, H. Ghosh and N. Pradhan, *J. Phys. Chem. Lett.*, 2019, **10**, 1300–1305.
- 20 S. K. Mehetor, H. Ghosh and N. Pradhan, *ACS Energy Lett.*, 2019, **4**, 1437–1442.
- 21 Y. Liu, M. Siron, D. Lu, J. Yang, R. dos Reis, F. Cui, M. Gao, M. Lai, J. Lin, Q. Kong, T. Lei, J. Kang, J. Jin, J. Ciston and P. Yang, *J. Am. Chem. Soc.*, 2019, **141**, 13028–13032.
- 22 J. Liu, K. Song, Y. Shin, X. Liu, J. Chen, K. X. Yao, J. Pan, C. Yang, J. Yin, L. J. Xu, H. Yang, A. M. El-Zohry, B. Xin, S. Mitra, M. N. Hedhili, I. S. Roqan, O. F. Mohammed, Y. Han and O. M. Bakr, *Chem. Mater.*, 2019, **31**, 6642–6649.
- 23 M. A. Boles, M. Engel and D. V. Talapin, *Chem. Rev.*, 2016, **116**, 11220–11289.
- 24 H. A. Scheraga, *J. Biomol. Struct. Dyn.*, 1998, **16**, 447–460.
- 25 A. Sánchez-Iglesias, M. Grzelczak, T. Altantzis, B. Goris, J. Pérez-Juste, S. Bals, G. Van Tendeloo, S. H. Donaldson, B. F. Chmelka, J. N. Israelachvili and L. M. Liz-Marzán, *ACS Nano*, 2012, **6**, 11059–11065.
- 26 P. Atkins and J. de Paula, *Physical Chemistry for the Life Sciences*, 2nd Edition, W. H. Freeman, 2011.
- 27 G. Kresse and J. Furthmüller, *Comput. Mater. Sci.*, 1996, **6**, 15–50.
- 28 J. P. Perdew, K. Burke and M. Ernzerhof, *Phys. Rev. Lett.*, 1997, **78**, 1396–1396.
- 29 P. E. Blöchl, *Phys. Rev. B: Condens. Matter Mater. Phys.*, 1994, **50**, 17953–17979.
- 30 S. Grimme, *J. Comput. Chem.*, 2006, **27**, 1787–1799.
- 31 S. Grimme, J. Antony, S. Ehrlich and H. Krieg, *J. Chem. Phys.*, 2010, **132**, 154104.
- 32 K. Momma and F. Izumi, *J. Appl. Crystallogr.*, 2011, **44**, 1272–1276.
- 33 C. Wang, A. S. R. Chesman and J. J. Jasieniak, *Chem. Commun.*, 2017, **53**, 232–235.
- 34 W. Zhai, J. Lin, Q. Li, K. Zheng, Y. Huang, Y. Yao, X. He, L. Li, C. Yu, C. Liu, Y. Fang, Z. Liu and C. Tang, *Chem. Mater.*, 2018, **30**, 3714–3721.
- 35 C. Wang, A. S. R. Chesman, W. Yin, L. Frazer, A. M. Funston and J. J. Jasieniak, *J. Chem. Phys.*, 2019, **151**, 121105.
- 36 D. Landini and F. Rolla, *J. Org. Chem.*, 1980, **45**, 3527–3529.
- 37 A. Pan, B. He, X. Fan, Z. Liu, J. J. Urban, A. P. Alivisatos, L. He and Y. Liu, *ACS Nano*, 2016, **10**, 7943–7954.
- 38 D. Gidalevitz, Z. Huang and S. A. Rice, *Biophys. J.*, 1999, **76**, 2797–2802.
- 39 Z. Wang, X. D. Wen, R. Hoffmann, J. S. Son, R. Li, C.-C. Fang, D.-M. Smilgies and T. Hyeon, *PNAS*, 2010, **107**(40), 17119–17124.
- 40 L. Ramin and A. Jabbarzadeh, *Langmuir*, 2011, **27**, 9748–9759.
- 41 E. De La Llave, R. Clarenc, D. J. Schiffrin and F. J. Williams, *J. Phys. Chem. C*, 2014, **118**, 468–475.
- 42 L. Salem, *J. Chem. Phys.*, 1962, **37**, 2100–2113.
- 43 A. Antanovich, A. Prudnikau, A. Matsukovich, A. Achtstein and M. Artemyev, *J. Phys. Chem. C*, 2016, **120**, 5764–5775.
- 44 J. N. Israelachvili, *van der Waals Forces between Particles and Surfaces*, Elsevier, 2011.
- 45 F. Krieg, Q. K. Ong, M. Burian, G. Rainò, D. Naumenko, H. Amenitsch, A. Süess, M. J. Grotevent, F. Krumeich, M. I. Bodnarchuk, I. Shorubalko, F. Stellacci and M. V. Kovalenko, *J. Am. Chem. Soc.*, 2019, **141**, 19839–19849.
- 46 D. Baranov, S. Toso, M. Imran and L. Manna, *J. Phys. Chem. Lett.*, 2019, **10**, 655–660.
- 47 A. Chernikov, T. C. Berkelbach, H. M. Hill, A. Rigosi, Y. Li, O. B. Aslan, D. R. Reichman, M. S. Hybertsen and T. F. Heinz, *Phys. Rev. Lett.*, 2014, **113**, 1–5.
- 48 H. Huang, M. W. Feil, S. Fuchs, T. Debnath, A. F. Richter, Y. Tong, L. Wu, Y. Wang, M. Döblinger and B. Nickel, *Chem. Mater.*, 2020, **32**, 8877–8884.
- 49 N. M. Villegas, J. C. Hernandez, J. C. John and M. Sheldon, *Nanoscale*, 2023, **15**, 9728–9737.